

Enhanced Performance of Protonic Solid Oxide Steam Electrolysis Cell of Zr-Rich Side $\text{BaZr}_{0.6}\text{Ce}_{0.2}\text{Y}_{0.2}\text{O}_{3-\delta}$ Electrolyte with an Anode Functional Layer

Hajime Toriumi, SeongWoo Jeong, Sho Kitano, Hiroki Habazaki, and Yoshitaka Aoki*

Cite This: *ACS Omega* 2022, 7, 9944–9950

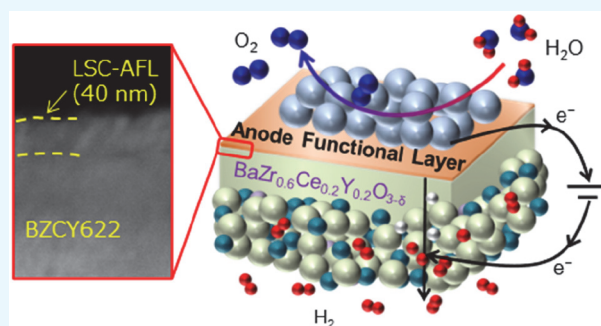
Read Online

ACCESS |

Metrics & More

Article Recommendations

ABSTRACT: Proton-conducting solid oxide electrolysis cells (H-SOEC) containing a 15- μm -thick $\text{BaZr}_{0.6}\text{Ce}_{0.2}\text{Y}_{0.2}\text{O}_{3-\delta}$ (BZCY622) electrolyte thin film, porous cathode cermet support, and $\text{La}_{0.6}\text{Sr}_{0.4}\text{Co}_{0.2}\text{Fe}_{0.8}\text{O}_{3-\delta}$ anodes were fabricated using a reactive cofiring process at approximately 1400 °C. Steam electrolysis was conducted by supplying wet air to the anode at a water partial pressure of 20 kPa. The performance was evaluated using electrochemical measurements and gas chromatography. At 600 °C, the cells generated an electrolysis current of 0.47 A cm^{-2} at a 1.3 V bias while the Faradaic efficiency reached 56% using 400 mA cm^{-2} . The electrolysis performance was efficiently improved by introducing a 40-nm-thick $\text{La}_{0.5}\text{Sr}_{0.5}\text{CoO}_{3-\delta}$ (LSC) nanolayer as an anode functional layer (AFL). The cells with LSC AFL produced an electrolysis current of 0.87 A cm^{-2} at a 1.3 V bias at 600 °C, and the Faradaic efficiency reached 65% under 400 mA cm^{-2} . Impedance analysis showed that the introduction of the AFL decreased the ohmic resistances and improved interfacial proton transfer across the anode/electrolyte interface and polarization resistances related to the anode reaction. These results demonstrate opportunities for future research on AFL to improve the performance of H-SOECs with Zr-rich $\text{BaZr}_x\text{Ce}_{1-x-y}\text{Y}_y\text{O}_{3-\delta}$ electrolytes.



1. INTRODUCTION

The development of sustainable energy technologies is driven by the growing interest to address current environmental and energy issues. Solar and wind power are considered primary sources of renewable energy; however, their potency as a reliable energy source is directly affected by several factors, such as climate and seasonality. Energy supply fluctuations can result in grid instability, particularly when the energy demand is higher than the current output. This issue is addressed by using grid-scale energy storage, which enables energy to be stored during peak production and be released during peak demand, thus transforming intermittent energy generators into grid-feasible resources. As such, large-scale green hydrogen production using water electrolysis has gained increasing popularity. The process generates hydrogen fuels that are subsequently stored in high-pressure tanks or converted to liquid fuels such as ammonia and methane. The three standard methods used in the process are (1) alkaline water electrolysis, (2) polymer electrolyte membrane water electrolysis, and (3) solid oxide steam electrolysis. The first two methods are carried out near room temperature using liquid water while the latter is carried out with steam and at high temperatures. It is found that the use of steam electrolysis, in lieu of water electrolysis, lowers the vaporization heat of the water

decomposition reaction. The theoretical voltage decreases from roughly 1.6 to 1.3 V as the temperature increases from 25 to 500 °C. Therefore, steam electrolysis by solid oxide electrolysis cells (SOECs) can be considered an alternative and highly efficient process to produce green hydrogen fuels using renewable energy.

Studies show that O^{2-} ion conductivity in yttria-stabilized zirconia (YSZ) is directly proportional to the process temperature.^{1,2} Thus, conventional SOECs using O^{2-} ion-conducting YSZ (O-SOECs) are operated at temperatures above 800 °C to meet the high activation energy requirement (~ 1 eV) to conduct O^{2-} ions in YSZ. However, the need for a high operating temperature leads to higher process costs and thermal degradation of materials.^{3–6} Recent studies are now focused on protonic or H^+ ion-conducting SOEC (H-SOECs) because of its ability to operate at lower temperatures compared to O-SOECs. The activation energy required for

Received: January 27, 2022

Accepted: February 28, 2022

Published: March 9, 2022



proton conductivity (~ 0.5 eV) is also observed to be lower in SOECs using H^+ -conducting $BaZr_xCe_{1-x-y}Y_yO_{3-\delta}$ (BZCY) perovskites relative to O-SOECs.^{7–15} Similarly, the use of Zr-rich-phase BZCY perovskites in steam electrolysis applications is advantageous since the material becomes more tolerant to CO_2 and H_2O as the Zr content increases.^{16,17} However, cells using such a Zr-rich phase exhibits lower performance compared to cells using a Ce-rich phase. This is due to the highly resistive nature of the grain boundary in the Y-doped $BaZrO_3$ moiety,¹⁸ which leads to substantial ohmic loss and interfacial polarization.¹⁹ Considering the process limitations, the development of highly efficient H-SOECs using a Zr-rich BZCY electrolyte with significantly lower interfacial resistance is significantly challenging. Tang et al. recently reported that the performance of H-SOECs using the $BaZr_xCe_{0.8-x}Y_{0.1}Yb_{0.1}O_{3-\delta}$ electrolyte in terms of ohmic loss and anode polarization resistance improves significantly by introducing several 10-nm-thick $La_{0.5}Sr_{0.5}CoO_{3-\delta}$ (LSC) anode functional layers (AFL) at the anode–electrolyte interface.²⁰ Although the proton conductivity of LSC is low in ambient atmospheres,²¹ AFL was found to promote interfacial proton transfer near the gas–anode–LSC triple phase boundary (TPB). Thus, the resistances related to proton incorporation from the anode to the electrolyte are reduced significantly. In this paper, we demonstrated that the LSC AFL can decrease both the interfacial proton transfer resistances and anode reaction resistances of H-SOEC with $BaZr_{0.6}Ce_{0.2}Y_{0.2}O_{3-\delta}$ (BZCY662). Consequently, the thin film cells with AFL gain about twice the electrolysis current as compared with the cells without AFL without lowering the Faradaic efficiency.

2. EXPERIMENTAL METHODS

2.1. Materials Preparation. Jeong et al. reported the fabrication of cermet anode-supported thin film fuel cells with BZCY622 electrolytes using a single-step cofiring process.²² In this experiment, BZCY622 thin film cells were also fabricated using a similar process. The raw mixture of BZCY622 was prepared by mixing stoichiometric amounts of $BaCO_3$ (High Purity Chemicals, 99.95%), CeO_2 (High Purity Chemicals, 99.99%), ZrO_2 (High Purity Chemicals, 98%), Y_2O_3 (High Purity Chemicals, 99.99%), and $Zn(NO_3)_2 \cdot 6H_2O$ (Wako Chemicals; 99.9%) additives as a sintering aid. The amount of additive was adjusted to a Zn/Ba molar ratio of 0.03. The starting materials were dispersed in ethanol, ball-milled for 24 h, and dried at 80 °C. A BZCY622 raw mixture and NiO were mixed in ethanol at a weight ratio of 40:60. After drying, the resultant mixed powders were uniaxially pressed under 20 MPa and isostatically pressed under a hydrostatic pressure of 100 MPa to obtain green pellets (12 mm ϕ , 1.6–1.8 mm d) for Ni-BZCY622 cermet cathode supports. The precursor layers of the electrolyte films were spin-coated on the green pellets using a MISAKA 1H-D7 spin coater. The slurry was prepared by dispersing the BZCY622 raw mixture in a solution containing a dispersant (20 wt % polyethylenimine ($M_w = 28\,000$) dissolved in α -terpineol) and a binder (5 wt % surfactant dissolved in α -terpineol) at a weight ratio of 10:3:1. The mixture was spin-coated once or twice on the surfaces of the green pellets at 3000 rpm for 30 s. After spin coating, the pellets were dried at room temperature and cofired at 1400 °C for 12 h to form half-cells. The backside of the sintered pellet was polished with SiC paper. The LSC AFL was deposited on the electrolyte surface by radio frequency (RF) magnetron sputtering with an LSC target. RF sputtering was performed at

a sputtering power of 50 W under a flow of 4% O_2/Ar gas at 50 sccm while the substrate temperature was maintained at 500 °C. Last, the $La_{0.6}Sr_{0.4}Co_{0.2}Fe_{0.8}O_{3-\delta}$ (LSCF) anode was screen-printed using an LSCF commercial ink (Fuel Cell Materials). The phase purity was checked by X-ray diffraction (XRD) analysis in the 2θ range between 20° and 80° at a scan rate of 5° min^{-1} using a Rigaku Ultima IV (Cu $K\alpha$ radiation). The microstructures of the fabricated cells were examined using a field emission scanning electron microscope (FESEM; SIGMA500, ZEISS) operated at 3 kV.

2.2. Electrochemical Measurements. Prior to conducting electrochemical measurements, the cathode side was exposed to a humidified 50% H_2/Ar gas mix at 700 °C for 6 h to convert NiO to metallic Ni and produce a porous Ni-BZCY622 cermet cathode. Steam electrolysis performance of cells was evaluated at 700 and 600 °C with a wet 10% H_2/Ar gas mix to the cathode and a 20% H_2O/air mix to the anode. The 20% H_2O/air mixture was prepared by passing air through a water bath maintained at approximately 60 °C and subsequently supplied to the anode chamber through a stainless-steel tube heated at 150 °C using a ribbon heater to prevent condensation. The I – V characteristics were measured using an electrochemical station (Biologic SP-300). The electrochemical impedance spectra of the SOECs were determined using a frequency response analyzer (Biologic SP-300) with a frequency range of 10^6 to 0.1 Hz and an AC amplitude of 30 mV. The hydrogen evolution rates (ν) in the cathode were quantified by analyzing the cathode exhaust gas using gas chromatography (490 Micro GC, Agilent Technologies). The Faraday efficiency, η , was calculated using the observed and theoretical hydrogen evolution rates (ν_{meas} and ν_{theo} , respectively) using the following equation:

$$\eta = \frac{\nu_{\text{meas}}}{\nu_{\text{theo}}} \times 100 = \frac{\nu_{\text{meas}}}{I \times (z \times F)^{-1}} \times 100 (\%) \quad (1)$$

where I is the applied current, z is the electron transport number of steam electrolysis, and F is Faraday's constant (96 485 C/mol).

3. RESULTS AND DISCUSSION

3.1. Morphology of Prepared Materials. Figure 1 shows the powder XRD pattern of pulverized thin film cell before

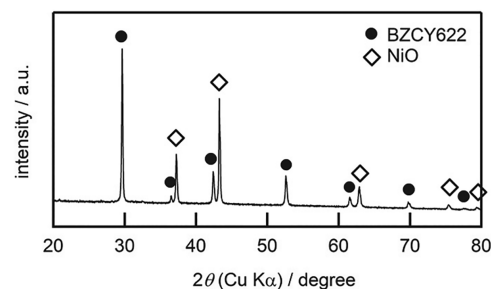


Figure 1. XRD pattern of pulverized half cells.

screen printing the LSCF anodes (half-cell). Results show that all of the peaks generated during the XRD analysis were from NiO and BZCY622 phases, while the BaY_2NiO_5 secondary phase²³ was not observed. This confirms that the reaction between BZCY622 and NiO to produce BaY_2NiO_5 does not occur.

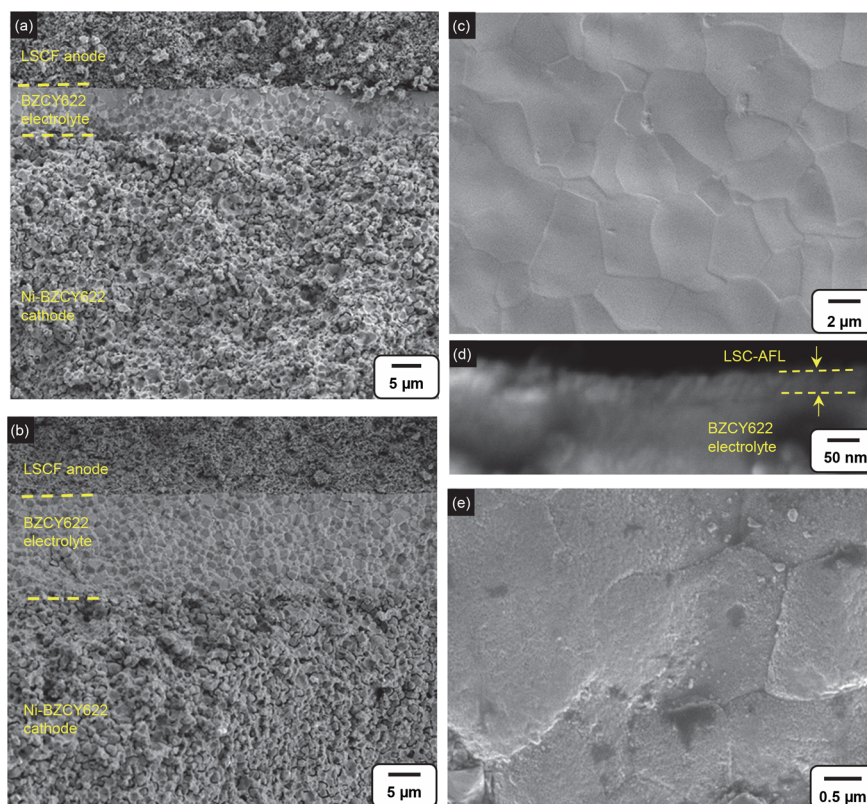


Figure 2. (a,b) Cross-sectional SEM image of cermet support H-SOEC with BZCY622 electrolyte films prepared by spin-coating (a) once and (b) twice. (c) Surface SEM image of BZCY622 electrolyte film prepared by once spin-coating. (d) Cross-sectional and (e) surface SEM images of LSC-AFL deposited on the BZCY622 electrolyte.

Figure 2a,b show the cross-sectional SEM images of H-SOEC with BZCY622 films prepared by spin-coating once and twice, respectively, after H_2 reduction of the cermet cathode. The cermet cathode is extremely porous with interconnected macropore networks that act as gas diffusion paths. The films prepared by spin-coating once and twice have a thickness of 15 and 30 μm , respectively, both of which are highly dense and formed uniformly over a porous cermet cathode. The LSCF anode is a porous layer composed of 50 nm diameter particles with a thickness of $\sim 40 \mu\text{m}$. Figure 2c shows the SEM image of the BZCY622 thin film bare surface on the porous Ni-BZCY662 cermet cathode after H_2 reduction at 700 $^\circ\text{C}$. The BZCY622 electrolyte layer maintains dense matrices without any crack formation and pinholes after reduction. This implies that the electrolyte film maintains adequate gas tightness. The BZCY622 grains grew up to 5 μm in diameter, which is larger than the BZCY622 grain size prepared by the sol-gel method.²⁴ Figure 2d and e show cross-sectional and surface SEM images of the LSC AFL on the BZCY622 thin film. The 40-nm-thick LSC layer, comprised of the nanoparticles with about 10 nm diameters, fully covers the electrolyte surface.

3.2. Electrochemical Measurements. Figure 3 shows the current–voltage (I – V) curves for the cell without the AFL, i.e., {20%– H_2O /air, LSCF | BZCY622 (15 μm) | Ni-BZCY622, wet 10% H_2 /Ar}, at 700 and 600 $^\circ\text{C}$. Open circuit voltage (OCV) at 700 and 600 $^\circ\text{C}$ are measured to be 0.84 and 0.91 V, respectively, which is lower than the ideal value of 0.93 and 0.96 V. The relatively low OCV value for the current cells must be attributed to the partial hole conductivity of BZCY622. On the basis of the theoretical OCV of 0.93 V as calculated by the Nernst equation, the proton transport number of BZCY622

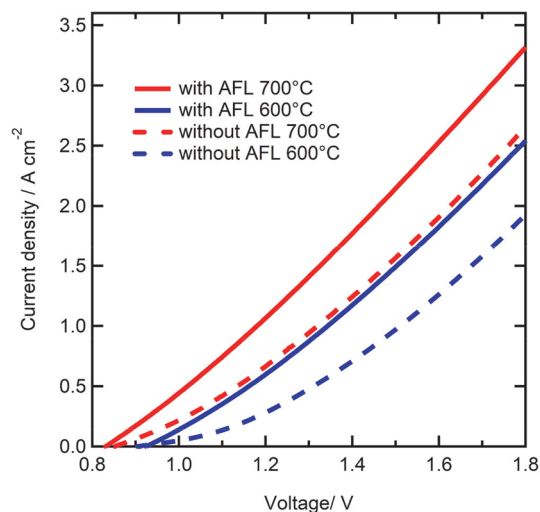


Figure 3. Performance (I – V curves) of the H-SOEC using 15- μm -thick BZCY622 film with and without LSC-AFL. Solid and dotted lines indicate the cell with and without LSC, respectively, and red and blue denote 700 and 600 $^\circ\text{C}$, respectively.

films can be roughly estimated to 0.89, which is in agreement with the proton transfer number of $\text{BaZr}_{0.7}\text{Ce}_{0.1}\text{Y}_{0.2}\text{O}_3$ (< 0.9)²⁵ at 700 $^\circ\text{C}$ under $pO_2 \geq 0.01$. This clearly indicates that leakage by hole conduction occurs on the BZCY662 thin film at a relatively high temperature.

The cells without AFL exhibited electrolysis currents of 0.92 and 0.47 A cm^{-2} at 700 and 600 $^\circ\text{C}$, respectively, at a 1.3 V bias. The OCV of the cell with AFL, i.e., {20%– H_2O /air, LSCF

| LSC/BZCY622 (15 μm) | Ni-BZCY622, wet 10% H_2/Ar }, is comparable to the results observed in cells without the AFL—OCV values are 0.82 and 0.92 V at 700 and 600 $^\circ\text{C}$, respectively. However, at 1.3 V, the electrolysis currents at 700 and 600 $^\circ\text{C}$ are 1.43 and 0.87 A cm^{-2} , respectively, which are nearly twice higher than the corresponding values of the cells without AFL. The electrolysis current of the cell with the LSC-AFL at 600 $^\circ\text{C}$ is similar to or higher than that of the H-SOECs using a Ce-rich side $\text{BaCe}_{1-x-y}\text{Zr}_x\text{M}_y\text{O}_3$ ($\text{M} = \text{Yb}, \text{Y}, \text{Co}; x \sim 0.1$) thin film electrolyte at 1.3 V under similar conditions.^{26–29}

Figure 4a,b show the AC impedance spectra for the cells of 15- μm -thick electrolyte with and without the AFL at 600 $^\circ\text{C}$ subjected to different DC conditions. In the H-SOECs spectra, the high-frequency x intercept is normally attributed to the electrolyte's ohmic resistances (R_O), while the succeeding arcs

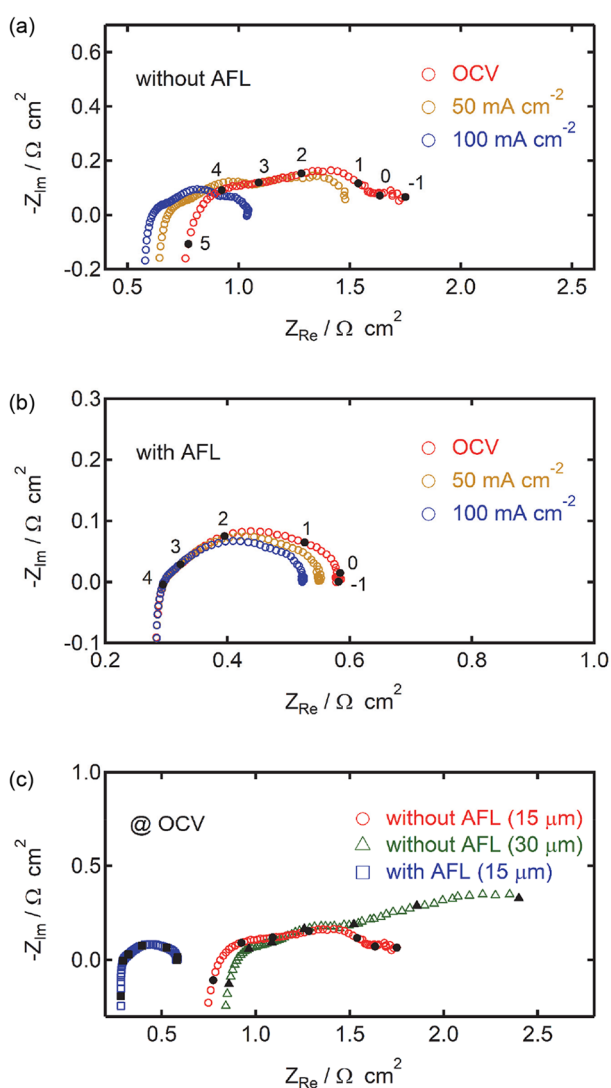


Figure 4. AC impedance spectra for H-SOEC of 15- μm -thick electrolyte (a) without and (b) with LSC-AFL, measured at 600 $^\circ\text{C}$ under various DC conditions. (c) AC impedance spectra of H-SOEC of 15- μm -thick electrolyte without (red, \circ) and with LSC-AFL (blue, \square) and of 30- μm -thick electrolyte without LSC-AFL (green, \triangle). In a–c, digits show the frequencies at each blackened point in the spectra.

denote the interfacial polarization mainly because of the anode reactions.^{30,31} The R_O of the cells without and with the AFL at 600 $^\circ\text{C}$ under OCV conditions are 0.81 $\Omega \text{ cm}^2$ and 0.30 $\Omega \text{ cm}^2$, respectively. This feature indicates that the R_O related to proton conduction efficiently decreases with the use of the AFL. Moreover, the R_O of H-SOEC was found to include the protonic resistances near the anode/electrolyte interfaces together with the bulk resistance of the electrolyte film. To separate interfacial resistance from bulk resistance of the electrolyte, the R_O is evaluated for the cells with different thicknesses of electrolyte films (Figure 4c). The R_O at 600 $^\circ\text{C}$ of the cell without AFL increases from 0.81 to 0.92 $\Omega \text{ cm}^2$ when the thickness of the electrolyte increases from 15 to 30 μm . Assuming the linear dependence of R_O on electrolyte thickness reveals the existence of an R_O of about 0.7 $\Omega \text{ cm}^2$ at zero thickness. Recent studies reported that proton-conducting solid oxide fuel cells (H-SOFCs) possess large impedances ($\sim 10^5$ Hz) due to slow proton transfer at the electrolyte–anode–gas TPB.^{32–36} On the basis of these, the BZCY622 cells involve relatively large resistances related to the interfacial proton transfer from the electrolyte to the anode. The value estimated for the zero thickness electrolyte cell without AFL, i.e., 0.7 $\Omega \text{ cm}^2$, is comparable to 80% of R_O for the 15- μm -thick electrolyte cell without AFL (0.81 $\Omega \text{ cm}^2$), which confirms that the interfacial resistances are a dominant component in the R_O of the BZCY622 base cells. The R_O for the 15- μm -thick electrolyte cells with AFL is only 0.30 $\Omega \text{ cm}^2$, which is much smaller than the value of the corresponding cell without AFL. These results unambiguously demonstrate that interfacial resistance is significantly reduced with the use of LSC–CFL.

The polarization resistances (R_p) are approximated using the total diameter of the impedance arcs. The calculated values for the cells without and with the AFL under OCV are 0.29 $\Omega \text{ cm}^2$ and 0.95 $\Omega \text{ cm}^2$, respectively. The R_p reduction caused by the AFL is more evident with the DC outputs. The R_p values with the AFL are 0.26 $\Omega \text{ cm}^2$ and 0.23 $\Omega \text{ cm}^2$ under a DC current of 50 and 100 mA cm^{-2} , respectively. These values are observed to be smaller by a factor of 0.33 and 0.53 than the values without the AFL. The results indicate that the LSC AFL can facilitate both interfacial proton transfer and other cathode reaction steps, such as charge transfer to adsorbed oxygen and/or oxygen desorption at the TPB.

The hydrogen production rate was calibrated using gas chromatography under galvanostatic electrolysis at 200 mA cm^{-2} and 400 mA cm^{-2} . Figure 5 illustrates the cell voltage transients, hydrogen evolution rate (v_{meas}), and Faradaic efficiency (η) at 600 and 700 $^\circ\text{C}$. The first electrolysis was conducted at 200 mA cm^{-2} for 30 min and at 400 mA cm^{-2} for 30 min subsequently. The voltages for cells without AFL are observed to be stable at 0.91 to 0.98 V during the electrolysis at 700 $^\circ\text{C}$ using 200 mA cm^{-2} and 400 mA cm^{-2} , respectively. Higher cell voltage is observed at 600 $^\circ\text{C}$ compared to the cell voltage at 700 $^\circ\text{C}$. This is primarily due to the increase in total cell resistance ($R_O + R_p$) with decreasing temperature. The cell voltage is 1.15 and 1.26 V at 200 mA cm^{-2} and 400 mA cm^{-2} , respectively. The nominal overpotentials, defined by the gap between the cell bias and the OCV, are equal to 0.24 and 0.36 for electrolysis at 600 $^\circ\text{C}$ in 200 mA cm^{-2} and 400 mA cm^{-2} , respectively.

v_{meas} achieves equilibrium within 20 min upon applying a constant current during electrolysis at 700 and 600 $^\circ\text{C}$. v_{meas} without the AFL is measured to be $3.6 \times 10^{-5} \text{ mol cm}^{-2} \text{ min}^{-1}$ and $6.9 \times 10^{-5} \text{ mol cm}^{-2} \text{ min}^{-1}$, and η values of 58% and 56%

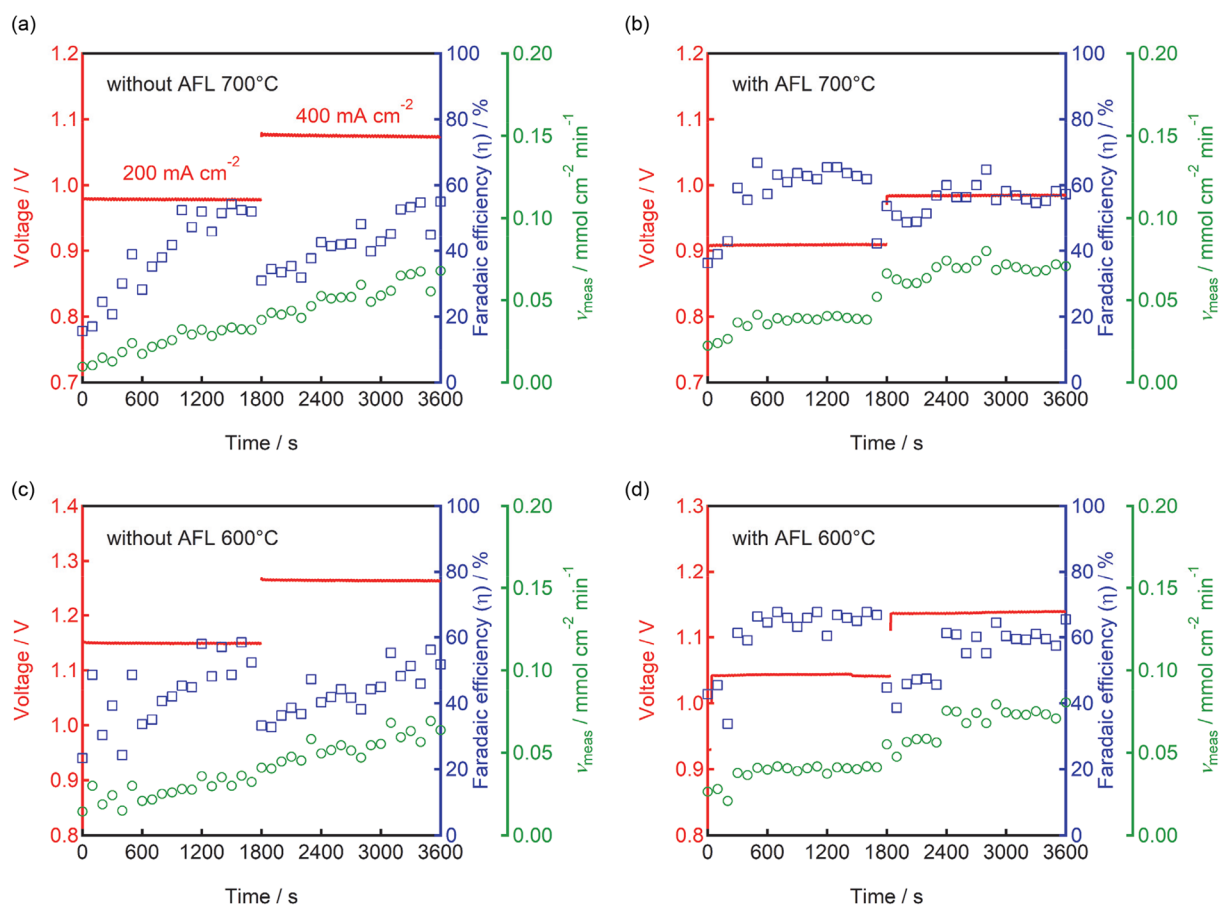


Figure 5. Faradaic efficiency (η ; blue, \square), hydrogen evolution rate (v_{meas} ; green, \circ) and cell voltage (red line) of (a,c) LSCF | BZCY622 ($15 \mu\text{m}$) | Ni-BZCY622 and (b,d) LSCF | LSC | BZCY622 ($15 \mu\text{m}$) | Ni-BZCY622 electrolysis cells at 600 and 700 °C under galvanostatic conditions at 200 and 400 mA cm^{-2} .

were acquired for electrolysis conducted at 600 °C using 200 mA cm^{-2} and 400 mA cm^{-2} , respectively. Similar results for v_{meas} and η at 700 °C are observed under equilibrium conditions. These η results are consistent with the values reported in previous studies for H-SOECs with an acceptor-doped $\text{Ba}(\text{Zr,Ce})\text{O}_3$ electrolyte.^{11–14,20,32,37–40} Vøllestad et al. determined the theoretical Faradaic efficiency of H-SOEC with $\text{BaZr}_{0.1}\text{Ce}_{0.7}\text{Y}_{0.1}\text{Yb}_{0.1}\text{O}_{3-\delta}$ under different hydrogen partial pressures (p_{H_2}) and water partial pressures ($p_{\text{H}_2\text{O}}$).⁴⁰ The approach employed numerical and experimental techniques and concluded that the efficiency is less than 70% when the anode's $p_{\text{H}_2\text{O}}$ and cathode's p_{H_2} are below 100 kPa. Hole carrier concentration in the electrolyte is also found above zero under similar conditions. These results confirm that the cells in this study conduct steam electrolysis and exhibited moderate Faradaic efficiency.

The cells with the LSC AFL exhibit stable voltages of 0.91 and 0.98 V at 700 °C for the galvanostatic electrolysis in 200 mA cm^{-2} and 400 mA cm^{-2} , respectively. In contrast, 1.04 and 1.14 V are observed at 600 °C under similar conditions. The cell overpotentials with the AFL at 600 °C are calculated to 0.12 and 0.21 for electrolysis under 200 mA cm^{-2} and 400 mA cm^{-2} , respectively. This is approximately 49 and 59%, respectively, of the corresponding values for cells without the AFL. v_{meas} with the AFL reaches $4.1 \times 10^{-5} \text{ mol cm}^{-2} \text{ min}^{-1}$ and $8.1 \times 10^{-5} \text{ mol cm}^{-2} \text{ min}^{-1}$ for electrolysis at 600 °C using 200 mA cm^{-2} and 400 mA cm^{-2} , respectively. The values are

comparable with the results for cells without the AFL. In addition, η values are 67 and 65% for electrolysis at 600 °C using 200 mA cm^{-2} and 400 mA cm^{-2} , respectively. These results demonstrate that LSC AFL lowers the overpotentials of H-SOEC efficiently by promoting interfacial proton transfer and anode reactions without increasing the hole leakage current. It was demonstrated in this study that the introduction of the AFL is an efficient way to improve the performance of H-SOEC-based Zr-rich side BZCY electrolytes. The results of this research demonstrate opportunities for future research on optimal AFL materials with excellent durability and high efficiency for H-SOECs.

4. CONCLUSIONS

The introduction of 40-nm-thick LSC AFL is a promising technique to decrease the ohmic and polarization resistances of H-SOECs with Zr-rich side BZCY622 electrolytes. The cell with the AFL can generate an electrolysis current of 0.87 A cm^{-2} at 600 °C at 1.3 V. This is nearly twice higher than that of the cell without the AFL. The cells without the AFL at 600 °C in OCV have ohmic resistance and polarization resistances of 0.81 $\Omega \text{ cm}^2$ and 0.95 $\Omega \text{ cm}^2$, respectively. Conversely, cells with the LSC AFL exhibited lower ohmic and polarization resistances of 0.30 $\Omega \text{ cm}^2$ and 0.29 $\Omega \text{ cm}^2$, respectively. The addition of AFL efficiently promoted interfacial proton transfer at the electrolyte/anode interface and corresponding anode

reactions. The current results offer a design concept for an efficient H-SOEC.

AUTHOR INFORMATION

Corresponding Author

Yoshitaka Aoki – Faculty of Engineering, Hokkaido University, Sapporo 060-8626, Japan; orcid.org/0000-0001-5614-1636; Email: y-aoki@eng.hokudai.ac.jp

Authors

Hajime Toriumi – Graduate School of Chemical Sciences and Engineering, Hokkaido University, Sapporo 060-8628, Japan

SeongWoo Jeong – Graduate School of Chemical Sciences and Engineering, Hokkaido University, Sapporo 060-8628, Japan

Sho Kitano – Faculty of Engineering, Hokkaido University, Sapporo 060-8626, Japan

Hiroki Habazaki – Faculty of Engineering, Hokkaido University, Sapporo 060-8626, Japan; orcid.org/0000-0002-7172-8811

Complete contact information is available at:

<https://pubs.acs.org/10.1021/acsomega.2c00569>

Funding

This work was supported by the JSPS KAKENHI Grant-in-Aid for Scientific Research (B), No. 21H02035 and KAKENHI Grant-in-Aid for Challenging Research (Exploratory), No. 21K19017.

Notes

The authors declare no competing financial interest.

ABBREVIATIONS

H-SOEC, proton-conducting solid oxide electrolysis cells; BZCY622, $\text{BaZr}_{0.6}\text{Ce}_{0.2}\text{Y}_{0.2}\text{O}_{3-\delta}$; LSC, $\text{La}_{0.5}\text{Sr}_{0.5}\text{CoO}_{3-\delta}$; AFL, anode functional layer; LSCF, $\text{La}_{0.6}\text{Sr}_{0.4}\text{Co}_{0.2}\text{Fe}_{0.8}\text{O}_{3-\delta}$

REFERENCES

- (1) Korte, C.; Peters, A.; Janek, J.; Hesse, D.; Zakharov, N. Ionic Conductivity and Activation Energy for Oxygen Ion Transport in Superlattices-The Semicohherent Multilayer System $\text{YSZ}(\text{ZrO}_2 + 9.5 \text{ mol\% Y}_2\text{O}_3)/\text{Y}_2\text{O}_3$. *Phys. Chem. Chem. Phys.* **2008**, *10*, 4623–4635.
- (2) Gerstl, M.; Friedbacher, G.; Kubel, F.; Hutter, H.; Fleig, J. The Relevance of Interfaces for Oxide Ion Transport in Yttria Stabilized Zirconia (YSZ) Thin Films. *Phys. Chem. Chem. Phys.* **2013**, *15*, 1097–1107.
- (3) Esquirol, A.; Brandon, N. P.; Kilner, J. A.; Mogensen, M. Electrochemical Characterization of $\text{La}_{0.6}\text{Sr}_{0.4}\text{Co}_{0.2}\text{Fe}_{0.8}\text{O}_3$ Cathodes for Intermediate-Temperature SOFCs. *J. Electrochem. Soc.* **2004**, *151*, A1847–A1855.
- (4) Ni, M.; Leung, M.; Leung, D. Technological Development of Hydrogen Production by Solid Oxide Electrolyzer Cell (SOEC). *Int. J. Hydrog. Energy* **2008**, *33*, 2337–2354.
- (5) Yang, X.; Irvine, J. T. S. $(\text{La}_{0.75}\text{Sr}_{0.25})_{0.95}\text{Mn}_{0.5}\text{Cr}_{0.5}\text{O}_3$ as the cathode of solid oxide electrolysis cells for high temperature hydrogen production from steam. *J. Mater. Chem.* **2008**, *18*, 2349–2354.
- (6) Matsui, T.; Kishida, R.; Kim, J. Y.; Muroyama, H.; Eguchi, K. Performance Deterioration of Ni-YSZ Anode Induced by Electrochemically Generated Steam in Solid Oxide Fuel Cells. *J. Electrochem. Soc.* **2010**, *157*, B776–B781.
- (7) Jeong, S.; Yamaguchi, T.; Okamoto, M.; Zhu, C.; Habazaki, H.; Nagayama, M.; Aoki, Y. Proton Pumping Boosts Energy Conversion in Hydrogen-Permeable Metal-Supported Protonic Fuel. *ACS Appl. Energy Mater.* **2020**, *3*, 1222–1234.
- (8) Stuart, P. A.; Unno, T.; Kilner, J. A.; Skinner, S. J. Solid Oxide Proton Conducting Steam Electrolysers. *Solid State Ionics* **2008**, *179*, 1120–1124.
- (9) Aoki, Y.; Nishimura, S.; Jeong, S.; Kitano, S.; Habazaki, H. Development of hydrogen-permeable metal support electrolysis cells. *ACS Appl. Energy Mater.* **2022**, *5*, 1385.
- (10) Leonard, K.; Lee, Y. S.; Okuyama, Y.; Miyazaki, K.; Matsumoto, H. Influence of Dopant Levels on the Hydration Properties of SZCY and BZCY Proton Conducting Ceramics for Hydrogen Production. *Int. J. Hydrog. Energy* **2017**, *42*, 3926–3937.
- (11) Zhu, H.; Ricote, S.; Kee, R. J. Faradaic efficiency in protonic-ceramic electrolysis cells. *J. Phys. Energy* **2022**, *4*, No. 014002.
- (12) Wang, W.; Medvedev, D.; Shao, Z. Gas Humidification Impact on the Properties and Performance of Perovskite-Type Functional Materials in Proton-Conducting Solid Oxide Cells. *Adv. Funct. Mater.* **2018**, *28*, 1802592.
- (13) Su, H.; Hu, Y. H. Degradation issues and stabilization strategies of protonic ceramic electrolysis cells for steam electrolysis. *Energy Sci. Eng.* **2021**, DOI: [10.1002/ese3.1010](https://doi.org/10.1002/ese3.1010).
- (14) Lei, L.; Zhang, J.; Yuan, Z.; Liu, J.; Ni, M.; Chen, F. Progress Report on Proton Conducting Solid Oxide Electrolysis Cells. *Adv. Funct. Mater.* **2019**, *29*, 1903805.
- (15) Chiara, A.; Giannici, F.; Pipitone, C.; Longo, A.; Aliotta, C.; Gambino, M.; Martorana, A. Solid–Solid Interfaces in Protonic Ceramic Devices: A Critical Review. *ACS Appl. Mater. Interfaces* **2020**, *12*, 55537–55553.
- (16) GUO, Y.; RAN, R.; SHAO, Z. Optimizing the modification method of zinc-enhanced sintering of $\text{BaZr}_{0.4}\text{Ce}_{0.4}\text{Y}_{0.2}\text{O}_{3-\delta}$ -based electrolytes for application in an anode-supported protonic solid oxide fuel cell. *Int. J. Hydrog. Energy* **2010**, *35*, S611–S620.
- (17) Sawant, P.; Varma, S.; Wani, B.N.; Bharadwaj, S.R. Synthesis, Stability and Conductivity of $\text{BaCe}_{0.8-x}\text{Zr}_x\text{Y}_{0.2}\text{O}_{3-\delta}$ as Electrolyte for Proton Conducting SOFC. *Int. J. Hydrog. Energy* **2012**, *37*, 3848–3856.
- (18) Lindman, A.; Helgee, E. E.; Wahnstrom, G. Comparison of Space-charge Formation at Grain Boundaries in Proton-conducting BaZrO_3 and BaCeO_3 . *Chem. Mater.* **2017**, *29*, 7931–7941.
- (19) Fabbri, E.; D'Epifanio, A.; Di Bartolomeo, E.; Licocchia, S.; Traversa, E. Tailoring the Chemical Stability of $\text{Ba}(\text{Ce}_{0.8-x}\text{Zr}_x)\text{Y}_{0.2}\text{O}_{3-\delta}$ Protonic Conductors for Intermediate Temperature Solid Oxide Fuel Cells (IT-SOFCs). *Solid State Ionics* **2008**, *179*, 558–564.
- (20) Tang, C.; Akimoto, K.; Wang, N.; Fadillah, L.; Kitano, S.; Habazaki, H.; Aoki, Y. Effect of Anode Functional Layer on Steam Electrolysis Performances of Protonic Solid Oxide Cells. *J. Mater. Chem. A* **2021**, *9*, 14032–14042.
- (21) Han, D.; Okumura, Y.; Nose, Y.; Uda, T. Synthesis of $\text{La}_{1-x}\text{Sr}_x\text{Sc}_{1-y}\text{Fe}_y\text{O}_{3-\delta}$ (LSSF) and measurement of water content in LSSF, LSCF and LSC hydrated in wet artificial air at 300 °C. *Solid State Ionics* **2010**, *181*, 1601–1606.
- (22) Jeong, S.; Kobayashi, T.; Kuroda, K.; Kwon, H.; Zhu, C.; Habazaki, H.; Aoki, Y. Evaluation of Thin Film Fuel Cells with Zr-Rich $\text{BaZr}_x\text{Ce}_{0.8-x}\text{Y}_{0.2}\text{O}_{3-\delta}$ Electrolytes ($x \geq 0.4$) Fabricated by a Single-Step Reactive Sintering Method. *RSC Adv.* **2018**, *8*, 26309–26317.
- (23) Tong, J.; Clark, D.; Bernau, L.; Sanders, M.; O'Hayre, R. Solid-State Reactive Sintering Mechanism for Large-Grained Yttrium-Doped Barium Zirconate Proton Conducting Ceramics. *J. Mater. Chem.* **2010**, *20*, 6333–6341.
- (24) Bi, L.; Shafi, S. P.; Traversa, E. Y-doped BaZrO_3 as a chemically stable electrolyte for proton-conducting solid oxide electrolysis cells (SOECs). *J. Mater. Chem. A* **2015**, *3*, 5815–5819.
- (25) Heras-Juaristi, G.; Pérez-Coll, D.; Mather, G. C. Temperature dependence of partial conductivities of the $\text{BaZr}_{0.7}\text{Ce}_{0.2}\text{Y}_{0.1}\text{O}_{3-\delta}$ proton conductor. *J. Power Sources* **2017**, *364*, 52–60.
- (26) Azimova, M. A.; McIntosh, S. On the Reversibility of Anode Supported Proton Conducting Solid Oxide Cells. *Solid State Ionics* **2011**, *203*, 57–61.

- (27) Kim, J.; Jun, A.; Gwon, O.; Yoo, S.; Liu, M.; Shin, J.; Lim, T.; Kim, G. Hybrid-Solid Oxide Electrolysis Cell: A New Strategy for Efficient Hydrogen Production. *Nano Energy* **2018**, *44*, 121–126.
- (28) Wu, W.; Ding, H.; Zhang, Y.; Ding, Y.; Katiyar, P.; Majumdar, P. K.; He, T.; Ding, D. 3D Self-Architected Steam Electrode Enabled Efficient and Durable Hydrogen Production in a Proton-Conducting Solid Oxide Electrolysis Cell at Temperatures Lower Than 600 °C. *Adv. Sci.* **2018**, *5*, 1800360.
- (29) Li, W.; Guan, B.; Ma, L.; Hu, S.; Zhang, N.; Liu, X. High Performing Triple-Conductive $\text{Pr}_2\text{NiO}_{4+\delta}$ Anode for Proton-Conducting Steam Solid Oxide Electrolysis Cell. *J. Mater. Chem. A* **2018**, *6*, 18057–18066.
- (30) Lin, J.; Chen, L.; Liu, T.; Xia, C.; Chen, C.; Zhan, Z. The Beneficial Effects of Straight Open Large Pores in the Support on Steam Electrolysis Performance of Electrode-Supported Solid Oxide Electrolysis Cell. *J. Power Sources* **2018**, *374*, 175–180.
- (31) Huan, D.; Shi, N.; Zhang, L.; Tan, W.; Xie, Y.; Wang, W.; Xia, C.; Peng, R.; Lu, Y. A New Efficient and Reliable Air Electrode Material for Proton Conducting Reversible Solid Oxide Cells. *ACS Appl. Mater. Interfaces* **2018**, *10*, 1761–1770.
- (32) He, F.; Wu, T.; Peng, R.; Xia, C. Cathode Reaction Models and Performance Analysis of $\text{Sm}_{0.5}\text{Sr}_{0.5}\text{CoO}_{3-\delta}$ – $\text{BaCe}_{0.8}\text{Sm}_{0.2}\text{O}_{3-\delta}$ Composite Cathode for Solid Oxide Fuel Cells with Proton Conducting Electrolyte. *J. Power Sources* **2009**, *194*, 263–268.
- (33) Wu, T.; Zhao, Y.; Peng, R.; Xia, C. Nano-sized $\text{Sm}_{0.5}\text{Sr}_{0.5}\text{CoO}_{3-\delta}$ as the cathode for solid oxide fuel cells with proton-conducting electrolytes of $\text{BaCe}_{0.8}\text{Sm}_{0.2}\text{O}_{2.9}$. *Electrochim. Acta* **2009**, *54*, 4888–4892.
- (34) Dailly, J.; Mauvy, F.; Marrony, M.; Pouchard, M.; Grenier, J.-C. Electrochemical properties of perovskite and A_2MO_4 -type oxides used as cathodes in protonic ceramic half cells. *J. Solid State Electrochem.* **2011**, *15*, 245–251.
- (35) Ricote, S.; Bonanos, N.; Rørvik, P. M.; Haavik, C. Microstructure and Performance of $\text{La}_{0.58}\text{Sr}_{0.4}\text{Co}_{0.2}\text{Fe}_{0.8}\text{O}_{3-\delta}$ Cathodes Deposited on $\text{BaCe}_{0.2}\text{Zr}_{0.7}\text{Y}_{0.1}\text{O}_{3-\delta}$ by Infiltration and Spray Pyrolysis. *J. Power Sources* **2012**, *209*, 172–179.
- (36) Jeong, S. W.; Wang, N.; Kitano, S.; Habazaki, H.; Aoki, Y. Metal/Oxide Heterojunction Boosts Fuel Cell Cathode Reaction at Low Temperatures. *Adv. Energy Mater.* **2021**, *11*, 2102025.
- (37) Duan, C.; Kee, R.; Zhu, H.; Sullivan, N.; Zhu, L.; Bian, L.; Jennings, D.; O'Hayre, R. Highly Efficient Reversible Protonic Ceramic Electrochemical Cells for Power Generation and Fuel Production. *Nat. Energy* **2019**, *4*, 230–240.
- (38) Lei, L.; Zhang, J.; Guan, R.; Liu, J.; Chen, F.; Tao, Z. Energy storage and hydrogen production by proton conducting solid oxide electrolysis cells with a novel heterogeneous design. *Energy Conversion. Management* **2020**, *218*, 113044.
- (39) Wrubel, J. A.; Gifford, J.; Ma, Z.; Ding, H.; Ding, D.; Zhu, T. Modeling the performance and faradaic efficiency of solid oxide electrolysis cells using doped barium zirconate perovskite electrolytes. *Int. J. Hydrog. Energy* **2021**, *46*, 11511–11522.
- (40) Vøllestad, E.; Strandbakke, R.; Tarach, M.; Catalán-Martínez, D.; Fontaine, M. L.; Beeaff, D.; Clark, D. R.; Serra, J. M.; Norby, T. Mixed Proton and Electron Conducting Double Perovskite Anodes for Stable and Efficient Tubular Proton Ceramic Electrolysers. *Nat. Mater.* **2019**, *18*, 752–759.